Dynamic Large Eddy Simulation of the Vortex Breakdown of Swirling Flow using MPI Parallel Technique

Hong Gye Sung*[1]

Dynamic Large Eddy Simulation과 MPI병렬 계산 기법을 이용한 스월 유동에서의 Vortex Breakdown에 관한 연구

성 홍 계

연소실 안으로 분출되는 스월 유동의 vortex breakdown mechanism에 대한 연구를 하였다. 3차원 유한 체적기법과 Runge-Kutta 시간 적분법이 적용되었으며, 난류모델은 dynamic large eddy simulation (DLES)이 적용되었다. 계산 시간의 효율성과 기억용량을 효과적으로 사용하기 위하여 message passing interface (MPI) 병렬계산 기법이 적용되었다. 스월 난류 유동에 있어서 vortex breakdown 거동을 가시적으로 표착 하였는데, 이는 스월 유동에 의한 난류 응력 증대, 난류 생성/소산율 증대 및 혼합율 증대에 대한 실험적 근거를 뒷받침하는 매우 중요한 결과이다. 또한 평균 속도와 난류 운동에너지에 대한 계산 결과도 실험 결과와 비교하였다.

Key Words: Large Eddy Simulation, Vortex Breakdown, Swirling Flow, MPI, Parallel Computing, CFD

1. Introduction

Swirling flows are used extensively in engineering applications, in particular, for flame stability and mixing in the combustion of gas-turbine engines. The flowfields of current practical interest in combustor primary zone involve regions of highly turbulent swirling and recirculating flows. Such regions can promote rapid fuel/air mixing and enhance flame stabilization, which lead to improve combustion efficiency, better blow-off limits, and a reduction in the formation of particulate and gasous pollutant.

Vortex breakdown is an important fluid phenomenon in swirling flows and has been widely researched since its discovery by Peckham & Atkinson[1] in an

* 2000년 9월 25일 접수

*1 Tech-4-2, Agency for Defense Development

investigation of the flow over "Gothic" wings. The vortex breakdown produces swirl-stabilized combustion systems[2]. At the end of center recirculation zone, the central forced processing vortex core inducing pressure and velocity fluctuation like swirl instability develops [3]. As the degree of swirl increases, the distance between the fuel and the fuel front as well as the flame length decreases [4]. Also the corner recirculation zone shortens significantly, which may contribute the length of the combustor shorten [5].

The suppression of combustion inducing pressure oscillations and the extension of flammability limits are a major challenge in the design and development of high performance combustors. For both passive and active control of combustion, it is common critical issue to build upon the physical understanding of turbulent shear layer and combustion dynamics to guide the development of effective active/passive control technology as combustion characteristics are closely related to detailed fluid dynamic processes. Thus, the physical understanding of vortical structures in a turbulent swirl is the major concern in this study.

2. Theoretical Formulation

The Favre averaged governing equations based on the conservation of mass, momentum, and energy for a compressible gas can be expressed with subgrid closure terms as;

$$\frac{\partial \bar{\rho}}{\partial t}+\frac{\partial}{\partial x_j}(\bar{\rho}\tilde{u}_j)=0 \tag{1}$$

$$\frac{\partial(\bar{\rho}\tilde{u}_j)}{\partial t}+\frac{\partial}{\partial x_j}(\bar{\rho}\tilde{u}_i\tilde{u}_j+\bar{p}-\tilde{\sigma}_{ij})=-\frac{\partial \tau_{ij}}{\partial x_j} \tag{2}$$

$$\frac{\partial(\bar{\rho}\tilde{E})}{\partial t}+\frac{\partial}{\partial x_j}[(\bar{\rho}\tilde{E}+\bar{p})\tilde{u}_j+\tilde{q}_j-\tilde{\sigma}_{ij}\tilde{u}_j] =-\frac{\partial}{\partial x_j}(C_P Q_j+V_j-D_j) \tag{3}$$

where a Favre-averaged variable is defined as $\tilde{f}=\overline{\rho f}/\bar{\rho}$. $\tilde{u}_j$, $\bar{\rho}$, and $\bar{p}$ are the filtered velocity, the filtered density, and the filtered pressure, respectively. $\tilde{E}=\tilde{\varepsilon}+\tilde{u}_i\tilde{u}_i/2$ is the filtered total energy per unit mass. And $\tilde{\sigma}_{ij}, \tilde{q}_j$ are the diffusive fluxes. The effect of the SGS terms appears through the SGS stresses τ_{ij} in momentum equation, as well as the SGS heat flux Q_j, the SGS turbulent diffusion $\partial V_j/\partial x_j$, and the SGS contribution to viscous diffusion $\partial D_j/\partial x_j$ in energy equation; these quantities are defined as,

$$\tau_{ij}=\bar{\rho}(\widetilde{u_i u_j}-\tilde{u}_i\tilde{u}_j) \tag{4a}$$

$$Q_j=\bar{\rho}(\widetilde{u_j T}-\tilde{u}_j\tilde{T}) \tag{4b}$$

$$V_j=\frac{1}{2}\bar{\rho}(\widetilde{u_j u_k u_k}-\tilde{u}_j\widetilde{u_k u_k}) \tag{4c}$$

$$D_j=\overline{\sigma_{ij}u_i}-\tilde{\sigma}_{ij}\tilde{u}_j \tag{4d}$$

2.1 Large eddy simulation

The compressible version of the dynamic Smagorinsky model (DSM) is employed in the present study. The anisotropic part of the SGS stresses is modeled using the Smagorinsky model[6], while the SGS energy τ_{kk} is modeled separately with a form proposed by Yoshizawa [7],

$$\tau_{ij}-\frac{\delta_{ij}}{3}\tau_{kk}=-C_R 2\overline{\Delta}^2\overline{\rho}\,|\tilde{S}|(\tilde{S}_{ij}-\frac{\delta_{ij}}{3}\tilde{S}_{kk})=C_R\alpha_{ij} \quad (5a)$$

$$\tau_{kk}=C_I 2\overline{\rho}\overline{\Delta}^2\,|\tilde{S}|^2=C_I\alpha \quad (5b)$$

where $\alpha_{ij}=-2\overline{\Delta}^2\overline{\rho}\,|\tilde{S}|(\tilde{S}_{ij}-\frac{\delta_{ij}}{3}\tilde{S}_{kk})$, $\alpha=2\overline{\rho}\overline{\Delta}^2\,|\tilde{S}|^2$, and C_R and C_I are model constants. The introduction of dynamic modeling ideas [8] has spurred significant progress in the subgrid-scale modeling of non-equilibrium flows. Moin *et al.* [9] proposed a modification of the eddy viscosity model (5a,b) in which the two model coefficients were determined dynamically, rather than input *a priori*. The dynamic model uses resolved scale information at the grid-filter level, and a coarser test-filter $\hat{G}$ with characteristic $\hat{\Delta}>\overline{\Delta}$, in order to compute the model parameters C_R and C_I as a function of space and time. The following expressions can be derived for the dynamic evaluation of C_R and C_I using the least square approach of Lilly [10] for the momentum SGS stress tensor.

$$C_R=\frac{<L_{ij}M_{ij}>}{<M_{kl}M_{kl}>}-\frac{1}{3}\frac{<L_{mm}M_{nn}>}{<M_{kl}M_{kl}>} \quad (6a)$$

$$C_I=\frac{<L_{kk}>}{<\beta-\hat{\alpha}>} \quad (6b)$$

The forms of L_{ij}, M_{ij} and β are given as follows:

$$L_{ij}=\widehat{\overline{\rho}\tilde{u}_i\tilde{u}_j}-\hat{\overline{\rho}}\tilde{\hat{u}}_i\tilde{\hat{u}}_j=\widehat{\overline{\rho u_i\rho u_j}/\overline{\rho}}-\widehat{\overline{\rho u_i}\,\overline{\rho u_j}}/\hat{\overline{\rho}} \quad (7a)$$

$$M_{ij}=\beta_{ij}-\hat{\alpha}_{ij} \quad (7b)$$

$$\beta_{ij}=-2\hat{\Delta}^2\hat{\overline{\rho}}\,|\tilde{\hat{S}}|(\tilde{\hat{S}}_{ij}-\frac{\delta_{ij}}{3}\tilde{\hat{S}}_{kk}) \quad (7c)$$

$$\beta=2\hat{\overline{\rho}}\hat{\Delta}^2\,|\tilde{\hat{S}}|^2 \quad (7d)$$

where over-hat represents the test-filtered variable, a Favre-filtered variable under test-filter is defined as $\tilde{\hat{f}}=\widehat{\overline{\rho f}}/\hat{\overline{\rho}}$. The brackets $<\cdot>$ denote an appropriate average to ensure numerical calculation stability[8,9].

The simplest approach is to use an eddy diffusivity model of the form.

$$Q_j=-\frac{\overline{\rho}\nu_T}{\mathrm{Pr}_T}\frac{\partial\tilde{T}}{\partial x_j}=-C_R\frac{\overline{\Delta}^2\overline{\rho}\,|\tilde{S}|}{\mathrm{Pr}_T}\frac{\partial\tilde{T}}{\partial x_j} \quad (8)$$

The turbulent Prandtl number Pr_T can be adjusted dynamically. The subtest scale heat flux is presented as

$$\Theta_j=\widehat{\overline{\rho u_j T}}-\hat{\overline{\rho}}\tilde{\hat{u}}_j\tilde{\hat{T}} \quad (9)$$

$$H_j=\Theta_j-\hat{Q}_j \quad (10)$$

The other two terms in the total energy equation (3) that require modeling are the SGS turbulent diffusion $\partial V_j/\partial x_j$ and the SGS viscous diffusion $\partial D_j/\partial x_j$. The only calculation that attempted to model the SGS turbulent diffusion was argued that $\tilde{u}_i\approx\tilde{\bar{u}}_i$ and proposed a model of the form $V_j=1/2\tilde{u}_i\tau_{ij}$. The SGS viscous diffusion is the smallest of the terms in the total energy equation. No model for this term has been proposed in the literature to date. In the present study, this term is negligible due to its small contribution to the energy budget.

2.2 Numerical Method

A three dimensional time-accurate scheme based on explicit Runge-Kutta time marching scheme and finite volume in space integration is used in this present work. At the inlet boundary, the velocity components in the *x*-,*y*-, and *z*-directions, mass flow rate, and local

temperature are specified. The x-directional velocity follows $1/7^{th}$ power based on the fully developed turbulent velocity profile, and azimuthal velocity is assumed to be proportional to the axial direction velocity by a factor of the tangent of the swirl vane angle. The physical turbulent inlet boundary conditions are provided by superimposing a time-dependent fluctuation onto a time-independent mean profile. The pressure is obtained by the one-dimensional momentum equation. For exit boundary conditions, the extrapolation of primitive variables may cause undesirable reflection waves. So, nonreflecting boundary conditions are applied. Further efficiency is obtained by implementing an MPI (Message Passing Interface) parallel computing architecture with a multi-block technique. Pentium II 450 MHz processors are clustered for parallel computation. For this study, the computational domain was decomposed in a general fashion to almost evenly divide grid points among the processors. The computational domain is composed of 28 blocks are assigned to each processor (i.e. a total of 28 processors). Although the processors share the work, the solution is independent of the number of processors used. The grid points on each processor are updated to the next time step simultaneously. In order to calculate the spatial derivatives near the processor's domain boundaries, the information in the overlap regions on each side of the local domain must be obtained from neighboring processors. This communication overhead is directly proportional to the volume-to-surface ratio of that subdomain. As is well known, the scale-up depends upon the problem size, and the optimization of the number of processors needs to be determined. But the number of processors used, in reality, may be hardware-dependent to speed up calculation by considering both execution and waiting times because 3D LES code handles a huge grid size. For example, there are about 1 million grids in this study. It is difficult to coordinate a sufficient number of processors to address the lengthy waiting time and/or the limitations of processor availability.

3. Results and Discussion

An experimental test conducted by the propulsion laboratory in Air Force was chosen as a calculation model due to the availability of experimental data [11]. The experiments were conducted in the axisymmetric dump combustor model shown in Fig. 1. The working fluid was air pushed through the model by a centrifugal-type blower. The swirler with 12 circular arc inlet guide vanes was located 50.8mm upstream of the dump plane. The leading edge of each blade was designed to be tangential to the incoming flow and perpendicular to the centerline of the combustor. The combustion chamber consisted of a Plexiglas pipe, 152.5mm I.D. and 1850mm long. A laser Doppler velocimeter (LDV) was used to measure the three velocity components and some turbulence quantities in different swirl numbers. The centerline velocity in the inlet pipe is 19.2 m/s and the inlet Reynolds number is 1.25×10^5, based on inlet radius. The swirl number in this experiment is defined as:

$$S = \int_{R_h}^{R_i} \overline{u}\,\overline{w} r^2 dr \Big/ \int_{R_h}^{R_i} R\overline{u}^2 r dr \qquad (11)$$

where R represents the radius of a combustor and subscripts h and i means swirl hub and inlet pipe, respectively. $\overline{u}$ and $\overline{w}$ are the mean velocity of axial and swirl velocity, respectively. The swirl number is 0.5.

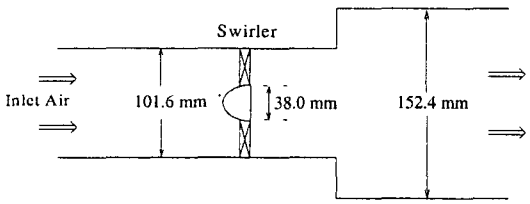

Fig. 1 Schematic of a model combustor with a swirl injector.

The computational domain consists of the inlet just after the swirler and the combustion chamber. The three-dimensional grid was generated by rotating the two-dimensional grid with respect to the combustor centerline, and the grid had $161 \times 75 \times 81$.

3.1 Swirl effects on mean velocity and turbulent kinetic energy

Comparisons of experimental data and computational results are presented in this section, and the physical characteristics of swirling flow are discussed in the next section. The computational and experimental data of mean axial and mean azimuthal (swirl) component velocity are compared at several measurement locations in Figs. 2 and 3. The symbol represents the experimental data, while a line shows the computational results obtained by averaging the values during flow throughout at each axial location. The nomenclature, H, represents the height of the backward facing step of the combustion chamber.

Fig. 2 shows that the axis of maximum axial component velocity shifts from the center to the wall with downstream distance due to the Coriolis force of the swirling effect. Axial recirculations of a central toroidal zone and a corner zone result from the swirling effect, which are fairly captured (see Figs. 2b and 2c). Swirl directional velocities also show acceptable results, even though the swirl velocity near the corner seems to be under-predicted (see Fig. 3). But the experimental data at this corner seems to be over-measured because the axial velocities are very low speed at this location close to the sidewall of the combustor (see Fig. 2a).

Fig. 4 shows the comparison of turbulent kinetic energy. The turbulent kinetic energy near the center toroidal recirculation zone is much greater than that near the corner recirculation zone. This result represents the major benefit of swirling inlet flow because one of the most significant and useful phenomena of swirl components produces strong shear and high turbulence near the toroidal recirculation zone. The tendency to overpredict turbulent kinetic energy near the shear layer of the central recirculation zone may be related to the lack of accuracy of the subgrid turbulence model used or inaccurate measurments in high turbulent shear region. Although a few discrepancies can be seen, the overall agreement is acceptable in view of complex turbulent swirling flow.

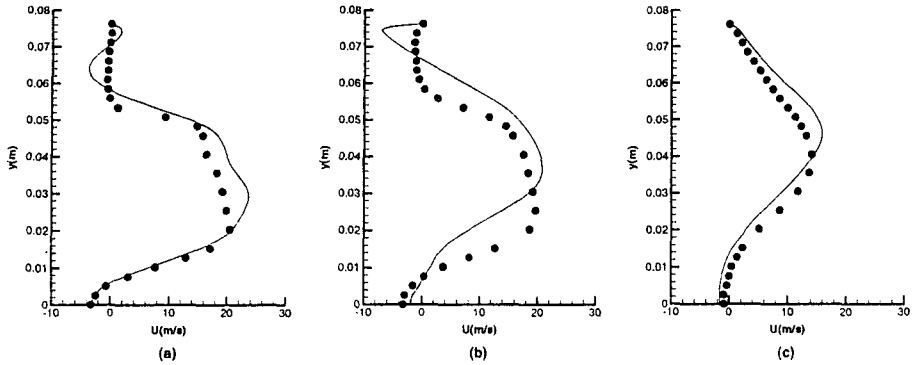

Fig. 2 Comparison of experimental and computational results of mean axial velocity at (a)X/H =0.38 (b) X/H=2.0 (c) X/H=4.0 (line:computation; symbol:experiment).

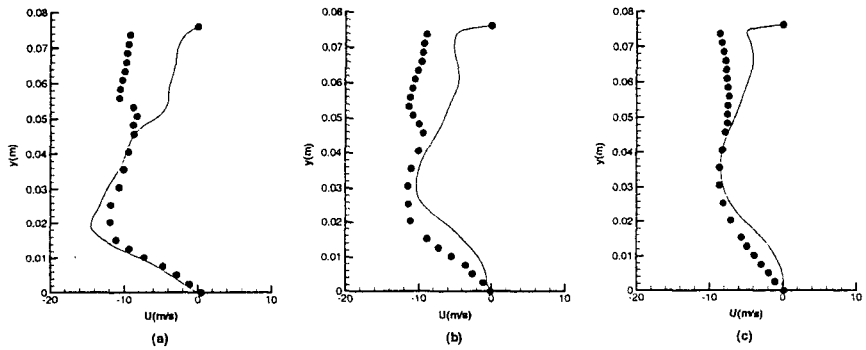

Fig. 3 Comparison of experimental and computational results of mean azimuthal velocity at (a)X/H =0.38 (b) X/H=2.0 (c) X/H=4.0 (line:computation; symbol:experiment).

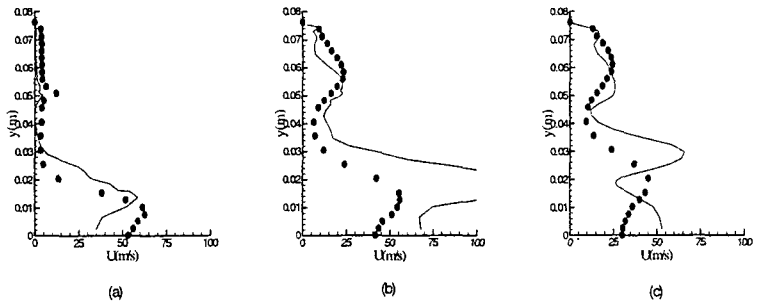

Fig. 4 Comparison of experimental and computational results of turbulent kinetic energy at (a)X/H =0.38 (b) X/H=2.0 (c) X/H=4.0 (line:computation ;symbol:experiment).

3.2 Swirl effects on vortex breakdown

The basic effect of a swirl results from the lateral momentum balance. For example, a high swirl significantly affects lateral pressure gradients given at any axial station from the lateral momentum balance, such as:

$$\frac{\partial p}{\partial r} = \frac{\rho w^2}{r} \tag{12}$$

The lateral pressure gradient increases the growth of the jet, resulting in reduction of combustion length. As the swirl velocities decay rapidly with downstream distance, the axial pressure gradient changes noticeably severely. Axial recirculation in the form of a central toroidal recirculation zone results eventually from the strong radial and axial pressure gradients.

Fig. 5 shows a three-dimensional view of the iso-surfaces of instantaneous pressure fluctuations, presenting a portion of the dilatation effect of turbulent structures. The individual vortical structures are shedding with highly distorted and unstructured shapes. The structures grow with increasing axial distance, caused by the pairing of individual vortices. The somewhat organized structures seen upstream are stretched highly toward azimuthal direction near the vortex breakdown region, and then stretched again to axial direction as swirl velocity decrease. Thus, azimuthal coherence may break rapidly. These phenomena can be explained by observing the vorticity equation. Axial circulation intensity is decreased in the x-direction, which may induce the divergence of radial vorticity and stream surfaces to conserve the angular momentum. From this postulate, it is hoped that some vorticity breakdown phenomena may be captured in the axial vorticity fields. As expected, process of vortices breakdown is vividly captured in the iso-surface field of the axial component of vorticity based on the mean flow field, as shown in Fig. 6. From Fig. 6, three important characteristics of swirling flow are visualized: diversity, decreasing strength of upstream vorticity, and vortex breakdown of turbulent swirling flow.

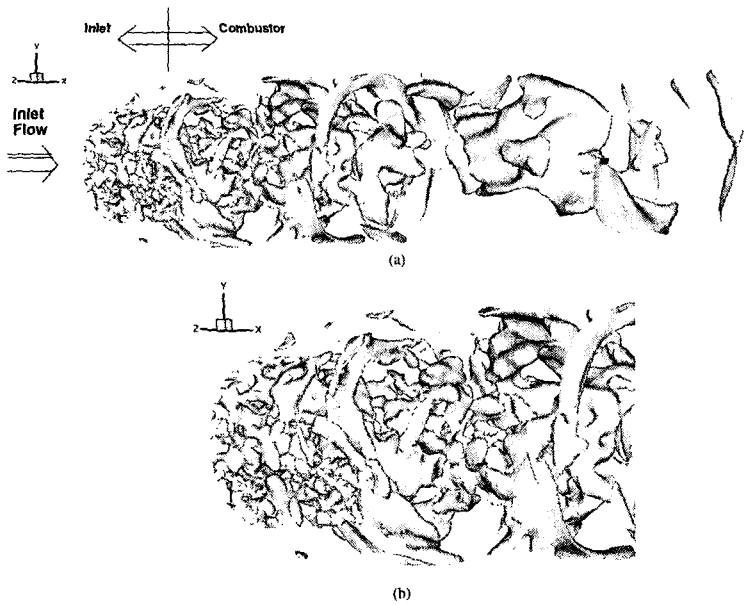

Fig. 5 Vortical structures visualized using iso-surfaces of instantaneous pressure fluctuations: entire domain (b) zoomed near the base of the combustor.

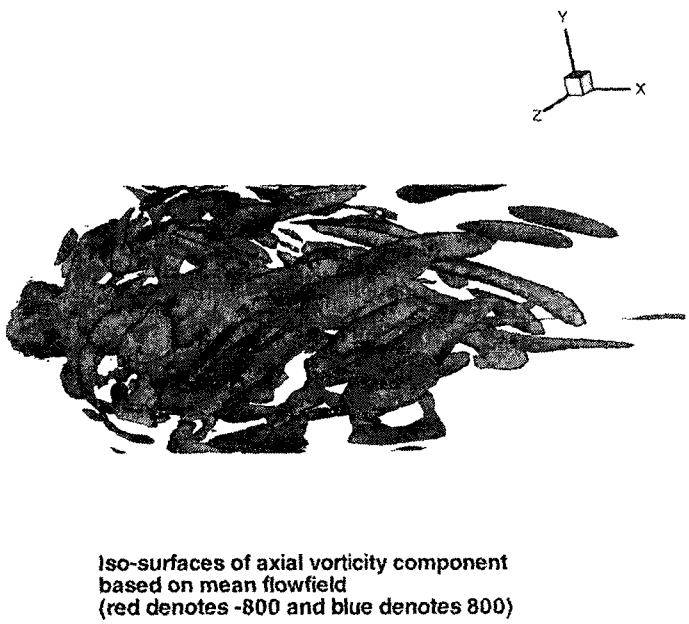

Fig. 6 Snapshot of iso-surface of axial vorticity component based on mean flowfield near the vorticity breakdown zone.

4. Conclusions

The swirling flow discharging into a combustion chamber was investigated using three-dimensional numerical analysis with an MPI (Message Passing Interface) parallel computing architecture. Large eddy simulation with dynamic subgrid scale (DSGS) model gained and visualized some insight into some fundamental phenomena, focusing on the fluid dynamics aspects of the process, including turbulent behaviors and vortex breakdown, which are related to combustion stability, air/fuel mixing and pollutant formation. The results showed the significant effects of swirl, diversity, decreasing strength of upstream vorticity, and vortex breakdown of turbulent swirling flow, which is usually used to stabilize the flame in real combustion chamber. Mean velocities are good agreement with experimental results corrected in insight. Although a few discrepancies can be seen, the overall agreement of turbulent kinetic energy is acceptable in view of complex turbulent swirling flow.

References

[1] Peckham, D. H. & Atkinson, S. A.."Preliminary Results of Low Speed Wind Tunnel Tests on a Gothic Wing of Aspect Ratio 1.0", *Aeronautical Research Council CP* 508, 1957.

[2] Lilley, D. G., "Swirl Flows in Combustion: a Review" *AIAA J.* 15, 1977, 1063-1077.

[3] Rhode, D. L., Lilley, D. G. & McLaughlin, D. K., "Mean Flowfields in Axisymmetric Combustor Geometries with Swirl", *AIAA J.* 21, 1983, 593-600.

[4] Dong, M. & Lilley, D. G., "Inlet Velocity Profile Effects on Turbulent Swirling Flow Predictions", *J. Propulsion Power* 10, 1994,155-160.

[5] So, R. M. C. & Ahmed, S. A., "Characteristics of Dump Combustor Flows", *Int. J. Heat Fluid Flow* 10, 1989,66-74.

[6] Smagorinsky, J. "General circulation experiments with the primitive equations: I. The basic experiment." *Mon. Weather Rev.* **91**, 99-164, 1963.

[7] Yoshizawa, A. "Statistical theory for compressible turbulent shear flows, with the applications to subgrid modeling." *Phys. Fluids* **29**, 2152-2164. 1986.

[8] Germano, M., Piomelli U., Moin, P., and Cabot, W., "A Dynamic Subgrid-Scale Eddy Viscosity Model," *Phys. Fluid* A 3(7), 1991.

[9] Moin, P., Squires, K., Cabot, W. & Lee, S. "A dynamic subgrid-scale model for compressible turbulence and scalar transport." *Phys. Fluids* **3**, 1991, 2746-2757.

[10] Lilly, D. K. 1992 A proposed modification of the Germano subgrid-scale closure model. *Phys. Fluids* **4**, 633.

[11] Favaloro, S. C., Nejad, A. S., Ahmed, S. A., Vanka, S. P. & Miller, T. J. 1989 An experimental and computational investigation of isothermal swirling flow in an axisymmetric dump combustor. *AIAA paper* 89-0620.